PROCEEDINGS OF SPIE

Sensitivity analysis for high-contrast imaging with segmented space telescopes

Lucie Leboulleux, Laurent Pueyo, Jean-François Sauvage, Thierry Fusco, Johan Mazoyer, et al.

SPIE.

Sensitivity analysis for high-contrast imaging with segmented space telescopes

Lucie Leboulleux[abc], Laurent Pueyo[a], Jean-François Sauvage[bc], Thierry Fusco[bc], Johan Mazoyer[ad], Anand Sivaramakrishnan[ad], Mamadou N'Diaye[e], Rémi Soummer[a]

[a] Space Telescope Science Institute, 3700 San Martin Drive, Baltimore, MD 21218, USA
[b] Aix Marseille Université, CNRS, LAM (Laboratoire d´Astrophysique de Marseille) UMR 7326, 13388, Marseille, France
[c] Office National d´Etudes et de Recherches Aérospatiales, 29 Avenue de la Division Leclerc, 92320 Châtillon, France
[d] Department of Physics and Astronomy, Johns Hopkins University, Baltimore, MD, USA
[e] Observatoire de Nice Côte d´Azur, Boulevard de l´Observatoire, 06304 Nice, France

ABSTRACT

Direct imaging and spectroscopy of Earth-like planets will require high-contrast imaging at very close angular separation: 1e10 star to planet flux ratio at a few tenths of an arcsecond. Large telescopes in space are necessary to provide sufficient collecting area and angular resolution to achieve this goal. In the static case, coronagraphic instrument designs combined with wavefront control techniques have been optimized for segmented on-axis telescope geometries, but the extreme wavefront stability required at very high contrast of the order of tens of picometers remains one of the main challenges. Indeed, cophasing errors and instabilities directly contribute to the degradation of the final image contrast. A systematic understanding is therefore needed to quantify and optimize the static and dynamic constraints on segment phasing. We present an analytical model: Pair-based Analytical model for Segmented Telescopes Imaging from Space (PASTIS), which enables quasi-instantaneous analytical evaluations of the impact of segment-level aberrations and phasing on the image contrast. This model is based on a multiple sum of Young interference fringes between pairs of segments and produces short and long exposure coronagraphic images with a segmented telescope in presence of local phase aberrations on each segment. PASTIS matches end-to-end numerical simulations with high-fidelity (3% rms error on the contrast). Moreover, the model can be inverted by dint of a projection on the singular modes of the phase to provide constraints on each Zernike polynomial for each segment. These singular modes provide information on the contrast sensitivity to segment-level phasing errors in the pupil, which can be used to derive constraints on both static and dynamic mitigation strategies (e.g. backplane geometry or segment vibration sensing and control). The few most sensitive modes can be well identified and must be controlled at the level of tens of picometers, while the least sensitive modes in the hundreds of picometers. This novel formalism enables a fast and efficient sensitivity analysis for any segmented telescopes, in both static and dynamic modes.

Keywords: Segmented telescope, cophasing, exoplanet, high-contrast imaging, error budget

1. INTRODUCTION

Achieving direct imaging and spectroscopy of Earth-like planets means being able to resolve smaller and fainter objects, a typical objective being to image planets with a 10^{-10} planet-to-star contrast and a 0.1 arcsec angular separation. Different solutions and tools have been developed to achieve this goal, such as sending telescopes to space (to null the impact of the atmospheric turbulence), increasing of the size of the primary mirror (to perform high-resolution images), combined with coronagraphs (to remove the starlight) and deformable mirrors (to perform wavefront control). To fit these large telescopes into the launch vehicle, they have to be folded and therefore segmented.

Further author information, send correspondence to Lucie Leboulleux: E-mail: leboulleux@stsci.edu, Telephone: 1 410 338 2881

Recent developments in coronagraphy and wavefront control start to absorb the effect of the diffraction due to the segmentation and to the spiders on the final image and contrast: for instance, apodized pupil Lyot coronagraphs (APLCs)[1–3] and Phase-Induced Amplitude Apodization (PIAA) coronagraphs[4] and the Active Compensation of Aperture Discontinuities (ACAD-OSM)[5,6] are now optimized to compensate for these effects. However, such solutions only correct for amplitude discontinuities and do not take into account the case where all segments are not perfectly aligned.

Indeed segmentation generates other issues, such as cophasing errors or segment unstabilities. Their impact on the coronagraphic Point Spread Function (PSF) quality needs to be studied, in particular to set up manufacturing and stability constraints for a viable mission. The traditional method is based on an end-to-end model of the optical system, on which a numerous amount of aberration phases are applied and propagated.[7,8] Because of the numerous factors that impact the contrast (local/global aberrations, phasing errors, segment vibrations, thermal drift...), this error budget is extremely time- and computer-consuming.

We developed a tool called the Pair-based Analytical model for Segmented Telescopes Imaging from Space (PASTIS) that enables a fast error-budget for any segmented pupil.[9,10] This model is mainly dedicated to space telescopes, such as the James Webb Space Telescope (JWST),[11,12] the Large Ultra-Violet Optical Infrared (LUVOIR) telescope[13,14] or the Habitable Exoplanet Imaging Mission (HabEx),[15] but can also been applied to ground-based segmented telescopes such as the Extremely Large Telescopes (ELTs).[16–19]

PASTIS enables to express directly the contrast of a coronagraphic image as a function of the Zernike coefficients of the segments' aberrations. This model can be inverted on the basis of the singular modes of the wavefront to directly provide the requirements in segment phasing, alignment, polishing, and stability to perform a target contrast. It was developed in a previous paper[10] in the static case where only one kind of Zernike polynomial is present on the segments. In this proceeding, we develop PASTIS to two other cases, more general: the general case where the segment-level aberrations are decomposed on several Zernike polynomials and the dynamic case, where the segments are impacted by vibrations that deteriorate the contrast.

Section 2 provides reminders about the PASTIS model and its main conclusions, for static errors of one single Zernike polynomial. This section also provides the basics for the developments of the next sections. In section 3, we extend this formalism to combinations of Zernike polynomials and apply it to segment phasing errors (piston, tip, and tilt). Finally in section 4, we develop PASTIS to dynamic segment aberrations, and apply it to the case of all segments vibrating at the same frequency.

2. REMINDERS ABOUT PASTIS FOR ONE SINGLE ZERNIKE POLYNOMIAL

The development of the Pair-based Analytical model for Segmented Telescopes Imaging from Space for one kind of Zernike polynomial applied on the pupil is described in a previosu paper.[10] This section consists of a summary of the main results of these papers, from the theoretical development of the model to its validation. It provides the needed basics for the extensions proposed further in this proceeding.

2.1 Theory

2.1.1 Hypotheses

We consider a segmented telescope, composed of identical segments. Behind the telescope, a coronagraph enables high-contrast imaging in the dark hole.

PASTIS is developed under different hypotheses.

First of all, we only consider small segment-level phase aberrations on the primary mirror. This means that:

- the amplitude aberrations are neglected

- other sources of aberrations such as downstream aberrations or the effect of the secondary mirror are also neglected

- global aberrations on the primary mirror of the telescope are sampled as a sum of segment-level aberrations[20]
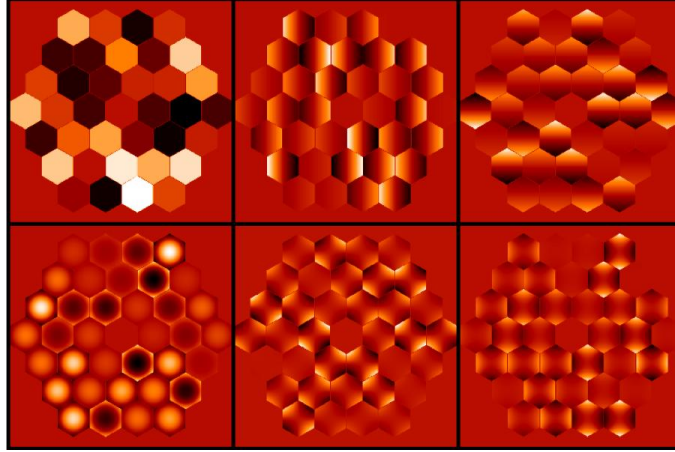
- we consider only residual phase errors.

Figure 1. Typical examples of phase errors for the section 2, where only one single Zernike polynomial is considered at a time. Top line from left to right: piston, tip, and tilt. Bottom line from left to right: focus, 45°-astigmatism, and 0°-astigmatism.

These hypotheses are kept in this entire proceeding.

Furthermore, in this section, the pupil phase aberrations are simplified to the case of one single Zernike polynomial present on the segments. For instance, it can correspond to segment-level piston aberrations only, if the segments are not well phased, or to segment-level focus aberrations only if the segments have focus-like polishing errors (See Fig. 1).

2.1.2 Expression of the model

The phase ϕ is expressed as a sum between the segment-level phases, each of them being expressed on the basis of Zernike polynomials $(Z_l)_{l \in [1, n_{zer}]}$ defined on a generic segment shape:

$$\phi(\mathbf{r}) = \sum_{l=1}^{n_{zer}} \sum_{k=1}^{n_{seg}} a_{k,l} Z_l(\mathbf{r} - \mathbf{r_k}), \tag{1}$$

where:

- n_{seg} is the number of segments

- $(a_{k,l})_{k \in [1, n_{seg}]}$ are the local Zernike coefficients of Z_l

- where $\mathbf{r}$ is the position vector in the primary mirror plane (pupil plane)

- $\mathbf{r_k}$ the position vector from the center of the pupil to the center of the k-th segment.

In this section, we simplify this formula using one single Zernike polynomial.

Furthermore, we approximate the intensity in the dark hole I as:

$$I(\mathbf{u}) = \left\| \widehat{\phi}(\mathbf{u}) \right\|^2 \tag{2}$$

where $\mathbf{u}$ is the position vector in the detector plane (focal plane) and $\hat{f}$ is the Fourier Transform of the function f.

We then obtain that the intensity in the dark hole is a sum of interference fringes, similar to the Young experiment, between all pairs of segment, modulated by a low-frequency envelope. This envelope depends only on the considered Zernike polynomial, defined on a segment.

$$I(\mathbf{u}) = \left\| \widehat{Z_l}(\mathbf{u}) \right\|^2 \times \left(\sum_{k=1}^{n_{seg}} c_{k,l}^2 a_{k,l}^2 + \sum_{k_1=1}^{n_{seg}} \sum_{k_2=1, k_2 \neq k_1}^{n_{seg}} c_{k_1,l} a_{k_1,l} c_{k_2,l} a_{k_2,l} \cos((\mathbf{r_{k_2}} - \mathbf{r_{k_1}}).\mathbf{u}) \right) \tag{3}$$
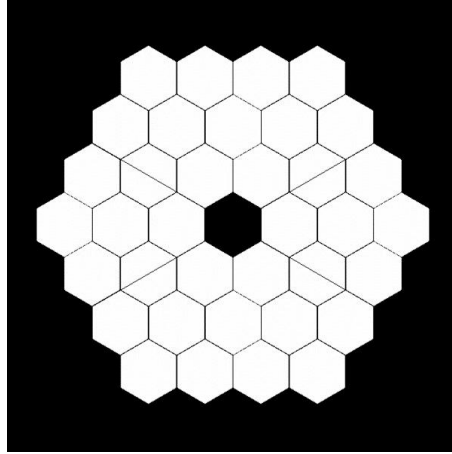
Figure 2. Pupil used for all applications in this proceeding, composed of 36 hexagonal segments. It is also one of the pupils of the Segmented Coronagraph Design and Analysis (SCDA) study.[3]

$(c_{k,l})_{k \in [1,n_{seg}]}$ are calibration coefficients, added here to take into account the coronagraph. They are obtained in a calibration step and strongly related to the apodization ratio of the segments.

This expression can be averaged to get the contrast in the dark hole:

$$C = C_0 + \sum_{k_1=1}^{n_{seg}} \sum_{k_2=1}^{n_{seg}} a_{k_1,l} a_{k_2,l} m_{k_1,k_2,l} \qquad (4)$$

where C_0 is the deep contrast of the coronagraph, ie. the best contrast the coronagraph can achieve, without aberrations, and $\forall (k_1,k_2) \in [1,n_{seg}]^2, m_{k_1,k_2,l} = \langle \left\| \widehat{Z}_l(\mathbf{u}) \right\|^2 c_{k_1,l} c_{k_2,l} \cos((\mathbf{r_{k_2}} - \mathbf{r_{k_1}}).\mathbf{u}) \rangle_{DH}, \langle f \rangle_{DH}$ corresponding to the mean value of the function f over the dark hole. This equation is equivalent to:

$$C = C_0 + A_l M_l A_l^t \qquad (5)$$

where the vector A_l contains all the coefficients $(a_{k,l})_{k \in [1,n_{seg}]}$, and $\forall (i,j) \in [1,n_{seg}]^2, M_l(i,j) = m_{i,j,l}$.

2.2 Application

2.2.1 Chosen application case

The PASTIS model is adaptable to all segmented pupils. For this proceeding, we choose to apply it to the 36-segment pupil presented in Fig. 2, with a monolithic source at 640nm.

It is combined with an Apodized Pupil Lyot Coronagraph (APLC) that enables a contrast of a few 10^{-11} in a dark hole between $4\lambda/D$ and $9\lambda/D$, without aberrations. The impact of the coronagraph on the final image is illustrated in Fig. 3.

In the application section, the end-to-end simulation corresponds to an explicit computation of the electric field from plane to plane using a Fourier formalism and the different masks composing the APLC.

2.2.2 Validation of PASTIS

In Fig. 4 we can find the contrasts computed from both PASTIS and the end-to-end simulation, for piston aberrations from 1pm to 10nm rms on the segments. For each rms piston value, 250 random phases are tested, providing 250 contrasts with the end-to-end simulation and 250 contrasts with PASTIS. From these two sets, we plot the minimum contrast, the maximum contrast, and the average contrast.

For all phases used for these curves, PASTIS provides an estimation of the contrast with an error around 3% rms. But the main advantage of PASTIS remains that the plots have been 10^7 times faster to obtain the the ones from the end-to-end simulation.
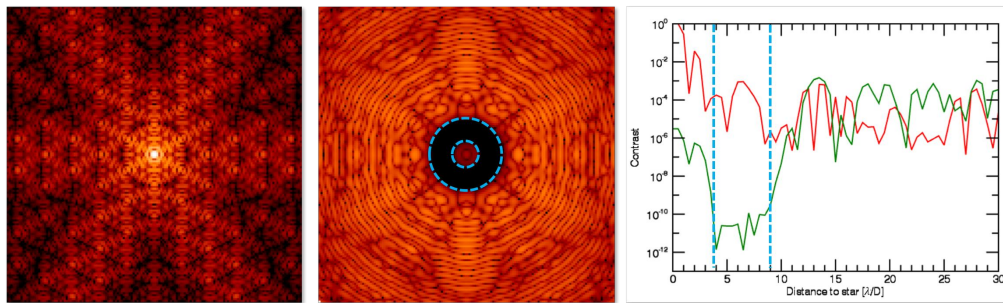
Figure 3. Left: PSF of the SCDA pupil (see Fig.2), obtained with an end-to-end numerical simulation with no coronagraph and aberrations. Center: PSF of the same SCDA pupil, obtained with an end-to-end numerical simulation with coronagraph and without aberrations. Right: Cut along the horizontal radius of the two previous PSFs (red: without APLC, green: with APLC). The two blue dashed lines correspond to the limits of the dark hole.
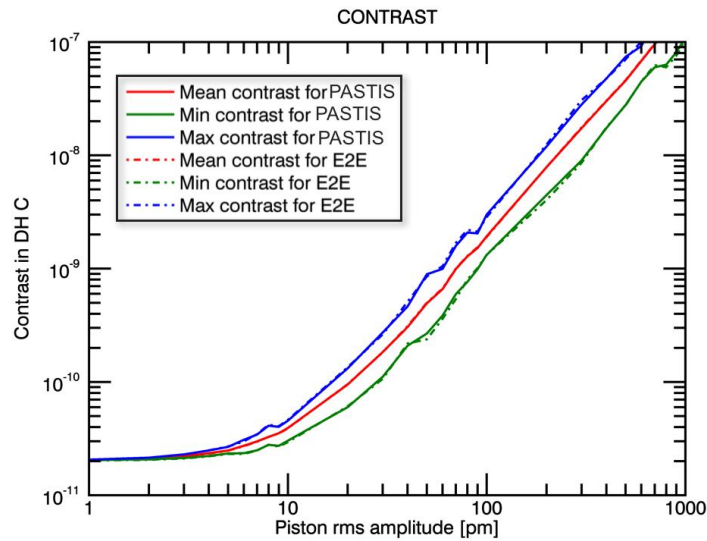

Figure 4. Contrast as a function of the rms piston aberrations on the segments. It was computed through two methods: the end-to-end model (dashed lines) and PASTIS (continuous lines). For each rms piston value, 250 random phases are selected, so 250 contrasts computed, and the minimum, average, and maximum values are plotted.
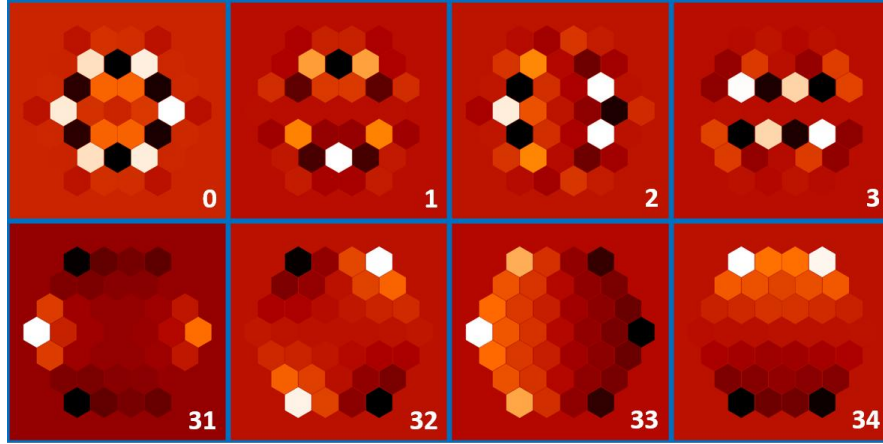
Figure 5. Some eigen modes in the piston case. Top: the four modes with the highest eigen values. We can notice that the segments the most concerned by these modes belong to the second ring, ie. are the least hidden by the coronagraph (apodizer and Lyot stop). Bottom: the four modes with the lowest eigen values. We can recognize discrete versions of low-order Zernike polynomials (astigmatisms, tip, and tilt).

As a comparison, similar results can be found in the studies of Stahl et al.,[21] later completed in Stahl et al.,[22] using end-to-end simulations.

2.3 Stability analysis

The objective of an error budget is to define constraints that enable to fulfill a certain performance. In our case, we want to set up constraints in terms of rms error on the segments to get a target contrast C. From Fig. 4 we can for instance derive from a target contrast the rms error for piston-like segments' phasing. However, we propose another approach, which takes into account the segment-dependant contribution to the contrast.

It is based on a projection of the phase on the eigen modes of the system. Indeed, by applying a Singular Value Decomposition (SVD) on the matrix M_l, we can obtain the eigen values $(\lambda_{p,l})_{p \in [1, n_{seg}]}$ and eigen modes $(U_{p,l})_{p \in [1, n_{seg}]}$ of the system. Fig. 5 illustrates a few modes issued from M_{piston}: the four modes with the highest eigen values (so impacting the contrast the most), and the four modes with the lowest eigen values (impacting the contrast the least). We can notice that the modes with the highest eigen values are made of aberrations located on the second ring of segments, ie. the least hidden by the optical components (apodizer and Lyot stop), while the modes with the lowest eigen values correspond to discretized global low order Zernike polynomials: the two astigmatisms (31 and 32) and the tip-tilt (33 and 34). It is known that in the design process, the apodizer has been optimized to be robust the tip-tilt misalignments, and this robustness is confirmed here. The 35-th mode, not represented in Fig. 5, has an almost null eigen value, and corresponds to a global piston of the primary mirror, which is known for not affecting the contrast.

The eigen modes form a basis of orthonormal vectors, so the final contrast due to a Zernike coefficients vector A is exactly the sum of the contrasts due to the projections of A on the different eigen modes:

$$C = \sum_{p=0}^{n_{seg}-1} C_p \tag{6}$$

Then, to get a contribution to contrast smaller than C_p on the p-th mode, the projection of the phase on this mode has to be smaller than

$$\sigma_p = \sqrt{\frac{C_p}{\lambda_{p,l}}}. \tag{7}$$

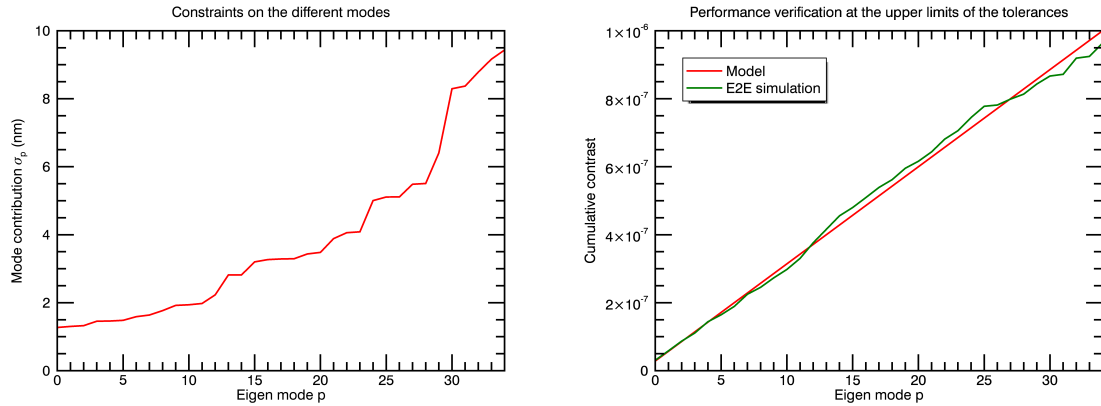We call σ_p the contribution of the phase to the mode p.[10]

Figure 6. Left: Contributions $(\sigma_p)_{p\in[0,n_{seg}-1]}$ on the different piston modes to reach a final target contrast of 10^{-6}, in the case where only local pistons on segments deteriorate the contrast. Right: Cumulative contrasts on these piston modes at their upper constraints to reach a final target contrast of 10^{-6}. In these two plots, only 35 modes are indicated, since the mode with a very low eigen value corresponds to a global piston on the pupil and is chosen to not contribute to the final contrast.

For applications, we consider that all modes contribute equally to the contrast, ie. all the C_p are equal, and that $C = 10^{-6}$. From the previous equation, we then derive the results of Fig. 6: (a) indicates the mode contributions $(\sigma_p)_{p\in[0,n_{seg}-1]}$ that generate such contrasts and (b) shows the cumulative contrasts generated by these constraints: both plots issued from PASTIS and the end-to-end simulation are almost linear and the error on the final contrast is 3.75%. We can conclude that this method to compute the tolerances is relevant.

3. ZERNIKE POLYNOMIAL COMBINATION

The previous section introduced the PASTIS model for a simple application case: the aberrations are static and composed of the same Zernike polynomial on all segments. In this new section, we study the case where the segment-level aberrations are more complex, being composed of several Zernike polynomials. As an example, we will focus on classic phasing errors, ie. a combination of piston, tip, and tilt aberrations.

3.1 Theory

We use the expression of the phase of Eq. 1, without simplifying it to the case of one single Zernike polynomial. We obtain in the general case:

$$\widehat{\phi}(\mathbf{u}) = \sum_{l=1}^{n_{zer}} \sum_{k=1}^{n_{seg}} a_{k,l} \widehat{Z}_l e^{-i\mathbf{r_k}\cdot\mathbf{u}} \tag{8}$$

Combining this equation and Eq 2 provides:

$$
\begin{aligned}
I(\mathbf{u}) &= \Big[\sum_{l_1=1}^{n_{zer}} \sum_{k_1=1}^{n_{seg}} a_{k_1,l_1} \widehat{Z}_{l_1} e^{-i\mathbf{r_{k_1}}\cdot\mathbf{u}}\Big] \times \Big[\sum_{l_2=1}^{n_{zer}} \sum_{k_2=1}^{n_{seg}} a_{k_2,l_2} \widehat{Z}_{l_2}^{\ *} e^{i\mathbf{r_{k_2}}\cdot\mathbf{u}}\Big] \\
&= \sum_{l_1=1}^{n_{zer}} \sum_{l_2=1}^{n_{zer}} \widehat{Z}_{l_1}.\widehat{Z}_{l_2}^{\ *} \sum_{k_1=1}^{n_{seg}} \sum_{k_2=1}^{n_{seg}} a_{k_1,l_1} a_{k_2,l_2} e^{i(\mathbf{r_{k_2}}-\mathbf{r_{k_1}})\cdot\mathbf{u}}
\end{aligned}
\tag{9}
$$

Since the intensity in the dark hole is real, $e^{i(\mathbf{r_{k_2}}-\mathbf{r_{k_1}})\cdot\mathbf{u}} = \cos((\mathbf{r_{k_2}} - \mathbf{r_{k_1}})\cdot\mathbf{u}) + i\sin((\mathbf{r_{k_2}} - \mathbf{r_{k_1}})\cdot\mathbf{u})$, and the envelopes $\widehat{Z}_{l_1}.\widehat{Z}_{l_2}^{\ *}$ are either real or imaginary, this expression is in practice sums of interference fringes between all pairs of segments, modulated by low-frequency envelopes.
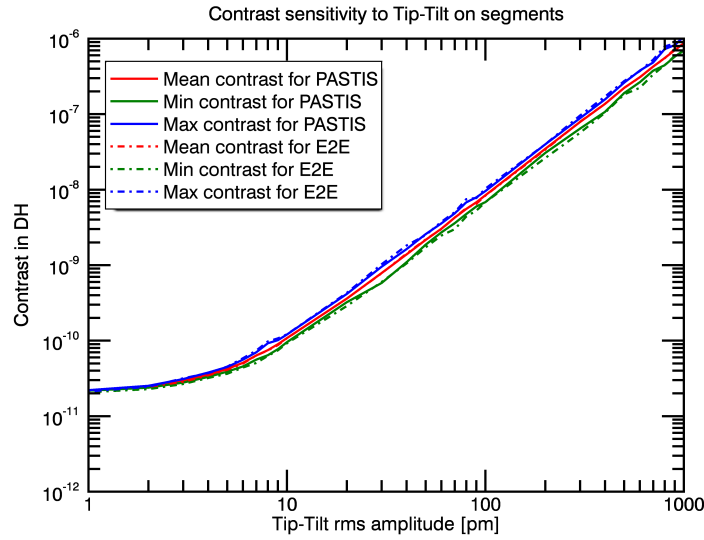
Figure 7. Contrast as a function of the rms piston-tip-tilt aberrations on the segments. It was computed through two methods: the end-to-end model (dashed lines) and PASTIS (continuous lines). For each rms value, 250 random phases are selected, so 250 contrasts computed, and the minimum, average, and maximum values are plotted.

By averaging this expression and taking the calibration coefficients $(c_{k,l})_{k \in [1, n_{seg}]}$ into account, we obtain:

$$C = C_0 + AMA^t \tag{10}$$

where:

$$
\begin{aligned}
A &= \begin{bmatrix} A_1 & ... & A_{n_{Zer}} \end{bmatrix} \\
&= \begin{bmatrix} a_{1,1} & ... & a_{n_{seg},1} & ... & a_{1,n_{Zer}} & ... & a_{n_{seg},n_{Zer}} \end{bmatrix} \\
M &= \begin{bmatrix} M_{1,1} & ... & M_{1,n_{Zer}} \\ & ... & \\ M_{n_{Zer},1} & ... & M_{n_{Zer},n_{Zer}} \end{bmatrix}
\end{aligned}
\tag{11}
$$

A is a concatenation of all the vectors A_l, while M is a block-diagonal matrix made of submatrices M_{l_1,l_2}, containing the coefficients:

$$
\begin{aligned}
M_{l_1,l_2}[k_1, k_2] &= m_{k_1,k_2,l_1,l_2} \\
&= c_{k_1,l_1} c_{k_2,l_2} \langle \widehat{Z_{l_1}} . \widehat{Z_{l_2}}^* e^{i(\mathbf{r_{k_2}} - \mathbf{r_{k_1}}) . \mathbf{u}} \rangle_{DH}
\end{aligned}
\tag{12}
$$

3.2 Application to the case of segment-level pistons, tips, and tilts

PASTIS in the case of Zernike polynomials' combination can be validated with a comparison with an end-to-end simulation. We use the same application case than described in section 2.2.1.

Fig. 7 provides a comparison between the results from PASTIS and from the end-to-end simulation, in the case of cophasing errors combining local piston, tip, and tilt errors on the segments. Like in Fig. 4, we plot here the minimum contrasts, the maximum contrasts, and the average contrasts computed from sets of 250 random phases, for sets from 1pm to 10nm rms. Once again, each contrast is computed with both techniques: PASTIS and the end-to-end simulation. As a conclusion, PASTIS still enables a huge gain of time for an error of around 9%.
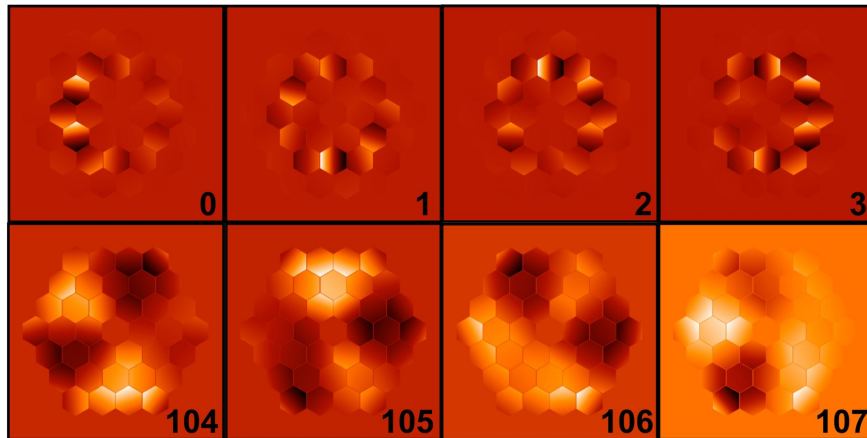
Figure 8. Some eigen modes in the piston-tip-tilt case. Top: the four modes with the highest eigen values. Tip and tilt errors appear to have a bigger impact on the contrast. Bottom: the four modes with the lowest eigen values, which correspond to low-order aberrations.

Once again, we can apply a Singular Value Decomposition on the matrix M enabling the computation of the contrast for piston, tip, and tilt aberrations. We can derive the 3×36 eigen modes of the chosen telescope. This information enables a better understanding of the phasing structures that deteriorate the contrast the most. It is then possible to optimize the backplane architecture or the sensitivity of specific edge sensors to avoid the dominant modes. For instance, Fig. 8 gives some of these eigen modes for the chosen telescope, the top ones corresponding to the ones with the highest eigen values, so impacting the contrast the most, and the bottom ones corresponding to the ones with the smallest eigen values, so impacting the contrast the least. We can deduce from this figure that the control of the tip-tilt on the second ring, mainly for one every two segments, is primordial. On the opposite, the last modes indicate that the coronagraph is highly resistant to global low-order aberrations. Such an information can be determinant when it comes to choose a coronagraph between several options providing otherwise similar performance.

Like in the one single Zernike polynomial case, it is also possible to quantify the relative importance of these eigen modes, or to obtain constraints to respect on each mode to achieve a target constraints. Fig. 9 provides for instance the constraints per mode to achieve a contrast of 10^{-6} in the dark hole. We can notice that the 40 first modes are quite equivalent in term of constraints (between 0.5nm and 1nm rms), while the modes higher than the 100th one seem negligible when it comes to cophasing (constraints higher than 8nm rms).

4. DYNAMICAL CASE EXTENSION

In the previous sections, only static aberrations were considered. However, multiple dynamical factors generate vibrations or segments' motions: cryocoolers, motors, thermal drifts, or even resonance effects. Therefore, we do not consider a snapshot image or an image obtained with static aberrations only, but an image integrated over an exposure time T_{exp}, obtained from successive images taken at a frame rate $F = 400$ Hz.

In this situation, PASTIS shows its main advantage. Indeed, the end-to-end simulation would require $T_{exp} \times F$ iterations to provide the contrast of one single long exposure image, while PASTIS, as we will see in this section, remains one single operation.

We also study one specific application, where all segments vibrate at the same frequency $f = 87.3$Hz around the flat position but with different amplitudes and phase delays.
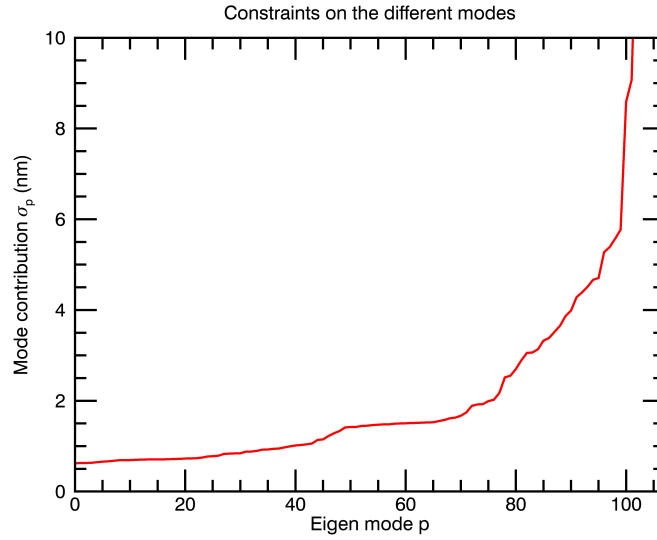
Figure 9. Contributions $(\sigma_p)_{p \in [0, n_{seg}-1]}$ on the different piston-tip-tilt modes to reach a final target contrast of 10^{-6}.

4.1 Theory for the generic case

In Eq. 5, we express the contrast as a function of the vector A_l, containing all the Zernike polynomial coefficients, and the matrix M_l which is a constant of the system. In the dynamical case, this equation becomes:

$$C(t) = C_0 + A_l(t)M_l A_l(t)^t$$
$$= C_0 + \sum_{k_1=1}^{n_{seg}} \sum_{k_2=1}^{n_{seg}} a_{k_1,l}(t) a_{k_2,l}(t) m_{k_1,k_2,l} \tag{13}$$

where t is the time variable. After a long exposure time, the integrated image has a contrast C in the dark hole that corresponds to the average of the contrasts of all the intermediate images.

$$C = \langle C(t) \rangle_{T_{exp}}$$
$$= C_0 + \sum_{k_1=1}^{n_{seg}} \sum_{k_2=1}^{n_{seg}} \langle a_{k_1,l}(t) a_{k_2,l}(t) \rangle_{T_{exp}} m_{k_1,k_2,l} \tag{14}$$

where T_{exp} is the exposure time.

4.2 Application to the case where all segments vibrate at the same frequency

4.2.1 Theory

In this case, all segments vibrate around the flat position:

$$\forall k \in [1, n_{seg}], a_{k,l}(t) = \tilde{a}_k cos(ft + \phi_k) \tag{15}$$

In the appendix A, it is demonstrated that:

$$\forall (k_1, k_2) \in [1, n_{seg}]^2, \langle a_{k_1,l}(t) a_{k_2,l}(t) \rangle_{T_{exp}} = \frac{cos(\phi_{k_1} - \phi_{k_2})}{2} \tilde{a}_{k_1} \tilde{a}_{k_2} \tag{16}$$
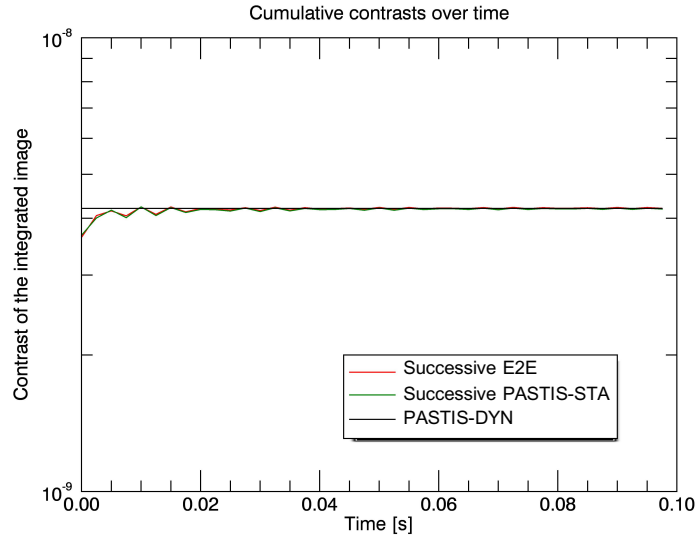
Figure 10. Example of temporal integration of the contrast, for piston-like vibrations. The segments vibrate at the frequency 87.3Hz and the amplitudes of the vibrations over all segments are 100pm. Furthermore: 1) to obtain the red curve, we compute the integrated PSF up to the time at the abscissa, then compute the contrast of this integrated PSF; this integrated contrast should converge towards the value computed in Eq. 17, 2) to obtain the green curve, we compute the contrast from the static PASTIS model at each time sample and average it up to the time at the abscissa, 3) the grey curve is constant and corresponds to the final contrast computed from Eq. 17.

Therefore, Eq. 14 becomes:

$$C = C_0 + \sum_{k_1=1}^{n_{seg}} \sum_{k_2=1}^{n_{seg}} \tilde{a}_{k_1} \tilde{a}_{k_2} \frac{cos(\phi_{k_1} - \phi_{k_2})}{2} m_{k_1,k_2,l}$$
$$= C_0 + \tilde{A} M' \tilde{A}^t$$

(17)

where $\tilde{A}$ contains all the vibration amplitudes $\tilde{a}_k$ and $\forall (i,j) \in [1, n_{seg}]^2, M'[i,j] = \frac{cos(\phi_i - \phi_j)}{2} M_l[i,j]$.

4.2.2 Application

We apply now this result for piston-like vibrations of frequency $f = 87.3$Hz. The vibration amplitudes $\tilde{A}$ are random but with an rms value of 100pm, and the vibration delays (ϕ_k) are random between $-\pi$ and π. The exposure time is $T_{exp} = 0.1$s. Also, we sample the time and consider that 400 images are taken by seconds. Fig. 10 and table 1 present the results:

- the red curves: we consider the PSF integrated up to the time t of the abscissa, which mean the average PSF of all previous successive PSFs. The red curve corresponds to the contrast of this intermediate integrated PSF at the time t. This computation method is also called "Successive E2E" in the table.

- the green curves: at the time t, we compute the contrasts of all images taken before thanks to the static PASTIS model as presented in section 2. The green curve corresponds to the average of these contrasts at the time t. This computation method is also called "Successive PASTIS-STA" in the table.

- the grey curves are constant and correspond to the dynamic contrasts computed thanks to Eq. 17.

In the ideal case, ie. for a 0% error on the estimation of the contrast, the red and green curves should converge towards the grey curves. In practice, in our cases we have 0.03% error.

We know from section 2.2.2 that there is a 3% error between the contrasts computed from end-to-end simulation and from PASTIS-STA, but the end-to-end simulations take 10^7 times longer to compute. Therefore, until

PASTIS-DYN	Successive PASTIS-STA	Successive E2E	Error between PASTIS-DYN and successive E2E	Error between PASTIS-DYN and successive PASTIS-STA
4.21×10^{-9}	4.20×10^{-9}	4.21×10^{-9}	0.03%	0.36%

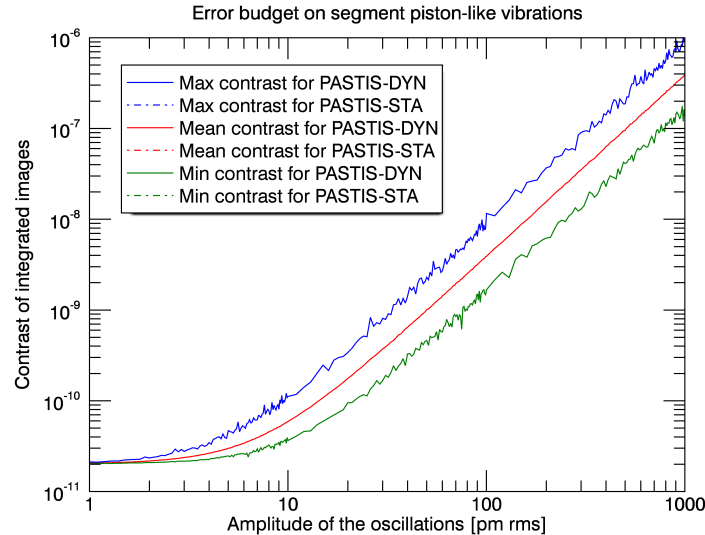Table 1. Contrasts and errors of the example introduced in Fig. 10.

Figure 11.   Contrast as a function of the rms piston-like vibrations on the segments. It was computed through two methods: the average of successive PASTIS-STA models (dashed lines) and the PASTIS-DYN model (continuous lines). For each rms value, 1000 random phases are selected.

the end of this section, we do not apply the end-to-end simulation anymore and compare PASTIS-DYN to the output of successive PASTIS-STA only, considering that successive PASTIS-STA provide outputs close enough to successive end-to-end simulations.

We now set $T_{exp} = 5$s. We consider random $\tilde{A}$, with rms values between 1 pm and 1 nm. For each rms value, we randomly pick 1000 different amplitudes $\tilde{A}$ and 1000 different phase delays' sets (ϕ_k). To each of these configurations of segments' vibrations, we apply 1) successive PASTIS-STA over the 5 seconds of T_{exp} and 2) PASTIS-DYN. For each rms value of $\tilde{A}$, we select the lowest contrasts computed with both methods, the mean contrasts, and the highest contrasts. Fig. 11 provides the results of this test: the outputs from PASTIS-DYN cannot be identified from the ones from the successive PASTIS-STA. To quantify the error of PASTIS-DYN compared to the output of successive PASTIS-STA, there is a $1.80 \times 10^{-5}\%$ rms error between the two mean curves, and for 1000 random sets of vibrations, the error between the outputs from PASTIS-DYN and successive PASTIS-STA is $8.30 \times 10^{-5}\%$ rms.

5. CONCLUSIONS

In this proceeding, we have introduced an analytical model called PASTIS. It was demonstrated in Leboulleux et al. (2017)[9] and Leboulleux et al. (2018)[10] in the case of one single static Zernike polynomial, summarized in section 2. This proceeding mainly extends the use of PASTIS to more complex situations: the segment-level aberrations are static combinations of several Zernike polynomials and dynamical effects such as vibrations also affect the system.

In the first of these two cases, we obtained a very good correlation between the results from the end-to-end simulation and PASTIS, with an rms error of around 9%. We could also identify the eigen modes of the phasing aberrations made of local piston, tip, and tilt and in particular the eigen modes that impact the contrast the

most. We could also quantify the relative impacts of these modes and provide absolute constraints to respect in order to maintain a target contrast.

As a second application case, we focused on segments' instabilities, in particular vibrations. When the temporal dimension is considered, PASTIS is particularly interesting, since it is extremely faster to compute than an end-to-end simulation. We noticed that this gain of computation time can be even more improved by reducing the successive contrast computations in one single operation, even after a long exposure time. We obtained very low errors in the contrasts when comparing the output of this one single operation (PASTIS-DYN), the average of the successive contrasts over time computed with PASTIS as presented in section 2 (PASTIS-STA), and the contrast of image obtained from successive end-to-end simulations and integrated over the exposure time (E2E).

In all theses cases, PASTIS provides not only a significant gain of time with a low error, but also a better comprehension of the system and its robustness. Knowing the eigen modes of the segmented primary mirror and their relative sensitivities to contrast enables to optimize the system, for instance the choice of edge sensors for segment's positioning or the architecture of the backplane structure.

Other parameters can also be optimized, such as the number of segments, their sizes and shapes, and the coronagraph itself, the objective being to get an optimal system that combines an absolute performance enabling exo-Earth imaging and a robustness to static and dynamic perturbations. PASTIS will enable a fast testing of these parameters in the path to make the next generation of space telescopes both performant and robust.

To diversify its applications and the used configurations, PASTIS is also currently being applied to the JWST for stability studies[23] and should be tested in laboratory on the High-contrast imager for Complex Aperture Telescopes (HiCAT) testbed at the Space Telescope Science Institute (STScI).[24]

ACKNOWLEDGMENTS

APPENDIX A.

We demonstrate here that $\forall (k_1, k_2) \in [1, n_{seg}]^2, \langle a_{k_1,l}(t) a_{k_2,l}(t) \rangle_{T_{exp}} = \frac{\tilde{a}_{k_1} \tilde{a}_{k_2}}{2} \cos(\phi_{k_1} - \phi_{k_2})$ for $T_{exp} >> 1/f$.

$$
\begin{aligned}
\langle a_{k_1,l}(t) a_{k_2,l}(t) \rangle_{T_{exp}} &= \frac{1}{T_{exp}} \int_0^{T_{exp}} \tilde{a}_{k_1} \tilde{a}_{k_2} \cos(f_{k_1} t + \phi_{k_1}) \cos(f_{k_2} t + \phi_{k_2}) \, \mathrm{d}t \\
&= \frac{1}{T_{exp}} \int_0^{T_{exp}} \tilde{a}_{k_1} \tilde{a}_{k_2} \frac{1}{2} (\cos(\phi_{k_1} - \phi_{k_2}) + \cos(2ft + \phi_{k_2} + \phi_{k_1})) \, \mathrm{d}t \\
&= \frac{\tilde{a}_{k_1} \tilde{a}_{k_2}}{2 T_{exp}} \left(\int_0^{T_{exp}} \cos(\phi_{k_1} - \phi_{k_2}) \mathrm{d}t + \int_0^{T_{exp}} \cos(2ft + \phi_{k_2} + \phi_{k_1})) \, \mathrm{d}t \right. \\
&= \frac{\tilde{a}_{k_1} \tilde{a}_{k_2}}{2 T_{exp}} (T_{exp} \cos(\phi_{k_1} - \phi_{k_2}) + 0)
\end{aligned}
\tag{18}
$$

since $T_{exp} >> 1/f$. We obtain:

$$
\langle a_{k_1,l}(t) a_{k_2,l}(t) \rangle_{T_{exp}} = \frac{\tilde{a}_{k_1} \tilde{a}_{k_2}}{2} \cos(\phi_{k_1} - \phi_{k_2})
\tag{19}
$$

REFERENCES

[1] Carlotti, A., Vanderbei, R., and Kasdin, N. J., "Optimal pupil apodizations for arbitrary apertures," *ArXiv e-prints* (Aug. 2011).

[2] N'Diaye, M., Pueyo, L., and Soummer, R., "Apodized Pupil Lyot Coronagraphs for Arbitrary Apertures. IV. Reduced Inner Working Angle and Increased Robustness to Low-order Aberrations," *Astrophysical Journal* **799**, 225 (Feb. 2015).

[3] Zimmerman, N. T., N'Diaye, M., St. Laurent, K. E., Soummer, R., Pueyo, L., Stark, C. C., Sivaramakrishnan, A., Perrin, M., Vanderbei, R. J., Kasdin, N. J., Shaklan, S., and Carlotti, A., "Lyot coronagraph design study for large, segmented space telescope apertures," in [*Space Telescopes and Instrumentation 2016: Optical, Infrared, and Millimeter Wave*], *Proc. SPIE* **9904**, 99041Y (July 2016).

[4] Guyon, O., Hinz, P. M., Cady, E., Belikov, R., and Martinache, F., "High Performance Lyot and PIAA Coronagraphy for Arbitrarily Shaped Telescope Apertures," *Astrophysical Journal* **780**, 171 (Jan. 2014).

[5] Pueyo, L. and Norman, C., "High-contrast Imaging with an Arbitrary Aperture: Active Compensation of Aperture Discontinuities," *Astrophysical Journal* **769**, 102 (June 2013).

[6] Mazoyer, J., Pueyo, L., N'Diaye, M., Fogarty, K., Leboulleux, L., Egron, S., and Norman, C., "Capabilities of ACAD-OSM, an active method for the correction of aperture discontinuities," *ArXiv e-prints* (Oct. 2017).

[7] Stahl, H. P., Postman, M., and Smith, W. S., "Engineering specifications for large aperture UVO space telescopes derived from science requirements," in [*UV/Optical/IR Space Telescopes and Instruments: Innovative Technologies and Concepts VI*], *Proc. SPIE* **8860**, 886006 (Sept. 2013).

[8] Stahl, M. T., Shaklan, S. B., and Stahl, H. P., "Preliminary analysis of effect of random segment errors on coronagraph performance," in [*Techniques and Instrumentation for Detection of Exoplanets VII*], *Proc. SPIE* **9605**, 96050P (Sept. 2015).

[9] Leboulleux, L., Sauvage, J.-F., Pueyo, L., Fusco, T., Soummer, R. N'Diaye, M., and St. Laurent, K., "Sensitivity analysis for high-contrast missions with segmented telescopes," in [*Techniques and Instrumentation for Detection of Exoplanets VIII*], *Proc. SPIE* **10400** (2017).

[10] Leboulleux, L., Sauvage, J. F., Pueyo, L., Fusco, T., Mazoyer, J., Soummer, R., Sivaramakrishnan, A., N'Diaye, M., and Fauvarque, O., "Pair-based Analytical model for Segmented Telescopes Imaging from Space (PASTIS) for sensitivity analysis," *Journal of Astronomical Telescopes, Instruments, and Systems (submitted)* (2018).

[11] Greenhouse, M. A., "The JWST science instrument payload: mission context and status," in [*Space Telescopes and Instrumentation 2016: Optical, Infrared, and Millimeter Wave*], *Proc. SPIE* **9904**, 990406 (July 2016).

[12] Clampin, M., "Status of the James Webb Space Telescope (JWST)," in [*Space Telescopes and Instrumentation 2008: Optical, Infrared, and Millimeter*], *Proc. SPIE* **7010**, 70100L (July 2008).

[13] Dalcanton, J., Seager, S., Aigrain, S., Battel, S., Brandt, N., Conroy, C., Feinberg, L., Gezari, S., Guyon, O., Harris, W., Hirata, C., Mather, J., Postman, M., Redding, D., Schiminovich, D., Stahl, H. P., and Tumlinson, J., "From Cosmic Birth to Living Earths: The Future of UVOIR Space Astronomy," *ArXiv e-prints* (July 2015).

[14] Pueyo, L., Zimmerman, N., Bolcar, M., Groff, T., Stark, C., Ruane, G., Jewell, J., Soummer, R., St. Laurent, K., Wang, J., Redding, D., Mazoyer, J., Fogarty, K., Juanola-Parramon, R., Domagal-Goldman, S., Roberge, A., Guyon, O., and Mandell, A., "The LUVOIR architecture "A" coronagraph instrument," in [*Society of Photo-Optical Instrumentation Engineers (SPIE) Conference Series*], *Society of Photo-Optical Instrumentation Engineers (SPIE) Conference Series* **10398**, 103980F (Sept. 2017).

[15] Mennesson, B., Gaudi, S., Seager, S., Cahoy, K., Domagal-Goldman, S., Feinberg, L., Guyon, O., Kasdin, J., Marois, C., Mawet, D., Tamura, M., Mouillet, D., Prusti, T., Quirrenbach, A., Robinson, T., Rogers, L., Scowen, P., Somerville, R., Stapelfeldt, K., Stern, D., Still, M., Turnbull, M., Booth, J., Kiessling, A., Kuan, G., and Warfield, K., "The Habitable Exoplanet (HabEx) Imaging Mission: preliminary science drivers and technical requirements," in [*Space Telescopes and Instrumentation 2016: Optical, Infrared, and Millimeter Wave*], *Proc. SPIE* **9904**, 99040L (July 2016).

[16] Macintosh, B., Troy, M., Doyon, R., Graham, J., Baker, K., Bauman, B., Marois, C., Palmer, D., Phillion, D., Poyneer, L., Crossfield, I., Dumont, P., Levine, B. M., Shao, M., Serabyn, G., Shelton, C., Vasisht, G., Wallace, J. K., Lavigne, J.-F., Valee, P., Rowlands, N., Tam, K., and Hackett, D., "Extreme adaptive optics for the Thirty Meter Telescope," in [*Society of Photo-Optical Instrumentation Engineers (SPIE) Conference Series*], *Proc. SPIE* **6272**, 62720N (June 2006).

[17] Kasper, M. E., Beuzit, J.-L., Verinaud, C., Yaitskova, N., Baudoz, P., Boccaletti, A., Gratton, R. G., Hubin, N., Kerber, F., Roelfsema, R., Schmid, H. M., Thatte, N. A., Dohlen, K., Feldt, M., Venema, L., and Wolf, S., "EPICS: the exoplanet imager for the E-ELT," in [*Adaptive Optics Systems*], *Proc. SPIE* **7015**, 70151S (July 2008).

[18] Davies, R., Ageorges, N., Barl, L., Bedin, L. R., Bender, R., Bernardi, P., Chapron, F., Clenet, Y., Deep, A., Deul, E., Drost, M., Eisenhauer, F., Falomo, R., Fiorentino, G., Förster Schreiber, N. M., Gendron, E., Genzel, R., Gratadour, D., Greggio, L., Grupp, F., Held, E., Herbst, T., Hess, H.-J., Hubert, Z., Jahnke, K., Kuijken, K., Lutz, D., Magrin, D., Muschielok, B., Navarro, R., Noyola, E., Paumard, T., Piotto, G., Ragazzoni, R., Renzini, A., Rousset, G., Rix, H.-W., Saglia, R., Tacconi, L., Thiel, M., Tolstoy, E., Trippe, S., Tromp, N., Valentijn, E. A., Verdoes Kleijn, G., and Wegner, M., "MICADO: the E-ELT adaptive optics imaging camera," in [*Ground-based and Airborne Instrumentation for Astronomy III*], *Proc. SPIE* **7735**, 77352A (July 2010).

[19] Quanz, S. P., Crossfield, I., Meyer, M. R., Schmalzl, E., and Held, J., "Direct detection of exoplanets in the 3-10 μm range with E-ELT/METIS," *International Journal of Astrobiology* **14**, 279–289 (Apr. 2015).

[20] Janin-Potiron, P., Martinez, P., and Carbillet, M., "Analytical decomposition of Zernike and hexagonal modes over an hexagonal segmented optical aperture," *Applied Optics (submitted)* (2018).

[21] Stahl, H. P., "Advanced Mirror Technology Development (AMTD) project: overview and year four accomplishments," in [*Advances in Optical and Mechanical Technologies for Telescopes and Instrumentation II*], *Proc. SPIE* **9912**, 99120S (July 2016).

[22] Stahl, M. T., Stahl, H. P., and Shaklan, S. B., "Contrast Leakage as a function of telescope motion," *Mirror Technology Days* (2016).

[23] Perrin, M., "Updated optical modeling of JWST coronagraph performance, contrast, and stability," in [*Space Telescopes and Instrumentation 2018: Optical, Infrared, and Millimeter Wave*], *SPIE paper 10698-8 in these proceedings* (2018).

[24] Soummer, R., "High-contrast imager for complex aperture telescopes (HiCAT): 5. rst results with segmented-aperture coronagraph and wavefront control," in [*Space Telescopes and Instrumentation 2018: Optical, Infrared, and Millimeter Wave*], *SPIE paper 10698-59 in these proceedings* (2018).